Article:
Collins, Sean M., Kepaptsoglou, Demie M. orcid.org/0000-0003-0499-0470, Hou, Jingwei et al. (5 more authors) (2020) Functional group mapping by electron beam vibrational spectroscopy from nanoscale volumes. Nano Letters. ISSN 1530-6984

https://doi.org/10.1021/acs.nanolett.9b04732

Functional group mapping by electron beam vibrational spectroscopy from nanoscale volumes

Sean M. Collins,[*, †, #] *Demie M. Kepaptsoglou,*[‡, §] *Jingwei Hou,*[†, ⊥] *Christopher W. Ashling,*[†] *Guillaume Radtke,*[||] *Thomas D. Bennett,*[†] *Paul A. Midgley,*[†] *and Quentin M. Ramasse*[‡, ¶]

[†]Department of Materials Science and Metallurgy, University of Cambridge, 27 Charles Babbage Road, Cambridge CB3 0FS, United Kingdom

[‡]SuperSTEM Laboratory, SciTech Daresbury Campus, Daresbury WA4 4AD, United Kingdom

[§]Department of Physics, University of York, Heslington, York YO10 5DD, United Kingdom

[||]Sorbonne Université, Muséum National d'Histoire Naturelle, UMR CNRS 7590, IRD, Institut de Minéralogie, de Physique des Matériaux et de Cosmochimie, IMPMC, 75005 Paris, France

[¶]School of Chemical and Process Engineering and School of Physics, University of Leeds, Leeds LS2 9JT, United Kingdom

KEYWORDS

Vibrational spectroscopy, electron energy loss spectroscopy, metal-organic frameworks, electron microscopy

ABSTRACT

Vibrational spectroscopies directly record details of bonding in materials, but spatially resolved methods have been limited to surface techniques for mapping functional groups at the nanoscale. Electron energy loss spectroscopy (EELS) in the scanning transmission electron microscope presents a route to functional group analysis from nanoscale volumes using transmitted sub-nanometer electron probes. Here, we now use vibrational EELS to map distinct carboxylate and imidazolate linkers in a metal-organic framework (MOF) crystal-glass composite material. Domains less than 100 nm in size are observed using vibrational EELS, with recorded spatial resolution <15 nm at interfaces in the composite. This nanoscale functional group mapping is confirmed by correlated EELS at core ionization edges as well as X-ray energy dispersive spectroscopy for elemental mapping of the metal centers of the two constituent MOFs. These results present a complete nanoscale analysis of the building blocks of the MOF composite and establish spatially resolved functional group analysis using electron beam spectroscopy for crystalline and amorphous organic and metal-organic solids.

Vibrational spectroscopies offer direct interrogation of the chemical bond. Infrared absorption and Raman spectroscopies probe molecular vibrations and phonons, capturing details of functional groups and lattice dynamics. Tip-enhanced scanning near field implementations have enabled vibrational spectroscopy approaching 10 nm spatial resolution[1] but are limited to studying the surface of a material. Recent advances in electron energy loss spectroscopy in the scanning transmission electron microscope (STEM-EELS) have enabled the observation of spectral signatures of phonons, molecular vibrations, and isotopes[2–8] by exploiting long range interactions with the electron beam. Experimental setups making use of electrons scattered to high angles[9] have also been used to evaluate the momentum-resolved dispersion of phonon modes in two-dimensional materials, including boron nitride and graphene lattices,[10,11] and to atomically resolved phonon mapping.[12,13] The possibilities for spatially resolved functional group mapping by vibrational STEM-EELS,[14] however, have not yet been fully realized.

In molecular systems, where the energy window currently accessible in STEM-EELS lends itself to fingerprinting organic moieties found in the classical mid-infrared (IR) energy range, long range interactions have enabled 'aloof' spectroscopy with reduced electron beam induced damage to the sample but for which spatial information is limited.[3,15] Understanding variations in bonding at the nanoscale in molecular and metal-organic solids requires spatially resolved measurements of characteristic vibrations. Here, we present spatially resolved STEM-EELS mapping of functional group vibrations within the volume of a metal-organic framework crystal glass composite (MOF CGC) with <15 nm spatial resolution and correlated elemental analysis. This approach unambiguously identifies the specific molecular vibrations arising from multiple organic ligands in the sample as well as the different metal centers present in crystalline and glassy domains.

MOFs, constructed from metal centers that are coordinated by organic linker molecules, often form part of a composite material for incorporation into applied materials and devices.[16] Recent work has established that zeolitic imidazolate frameworks (ZIFs), a broad class of MOFs, can be transformed to amorphous networks while retaining local coordination, such as through the formation of melt-quenched glasses.[17,18] These materials, including amorphous materials and coordination polymer crystals with large unit cells, contrast sharply with the materials which have been the focus of previous vibrational EELS studies. Characterization approaches that analyze the full sample volume, such as NMR techniques, have been successfully demonstrated to describe the typical coordination features preserved in MOFs and MOF composites.[19] However, these 'ensemble' measurements miss fine-scale details at individual interfaces in the material in favor of a description of the average properties. For Co-based ZIFs, optical signatures of tetrahedral coordination in the glass phase have been demonstrated using STEM-EELS, but this type of valence EELS depend on a particular, known optical signature for Co *d-d* transitions.[20] Vibrational analysis offers a generalizable route for nanoscale functional-group and ligand-specific characterization of MOFs and MOF interfaces.

MOF CGCs composed of MIL-53 [Al(OH)(BDC)] (BDC = 1,4-benzenedicarboxylate, $[O_2C\text{-}C_6H_4\text{-}CO_2]^{2-}$) and amorphous ($a_g$) ZIF-62 $[Zn(Im)_{1.75}(bIm)_{0.25}]$ (Im = imidazolate, $C_3H_3N_2^-$, bIm = benzimidazolate, $C_7H_5N_2^-$) have been shown to stabilize crystalline phases otherwise only observed at elevated temperatures[19] with a net improvement in gas sorption capacity.[21] The composite glass prepared from a ratio of 1:3 MIL-53 and ZIF-62, referred to as $(MIL\text{-}53)_{0.25}(a_g ZIF\text{-}62)_{0.75}$, contains <100 nm MIL-53 particles preserved in the high temperature open-pore crystal structure within an a_gZIF-62 matrix.[19] Tracking the locations of the distinct metal centers and linkers is essential for understanding the composite formation process.

Critically, *ab initio* spectroscopic calculations on amorphous systems of thousands of atoms are not readily feasible at present. These obstacles establish an imperative for experimental cross-validation approaches, achieved here by incorporating bulk Fourier-transform infrared (FTIR) spectroscopy, EELS at core ionization edges, and X-ray energy dispersive spectroscopy (EDS) mapping as well as mode assignments based on reference data and calculations, for a definitive demonstration of the functional group mapping capabilities of vibrational EELS on the nanometer scale.

Figure 1(a) presents a simplified schematic of the key features of the vibrational STEM-EELS experiment using a Nion Hermes microscope (SuperSTEM, UK). A 60 kV electron beam, monochromated to <30 meV (~240 cm^{-1}) full width at half maximum (FWHM) and focused to a sub-nanometer probe, is scanned across a sample. The transmitted electrons are dispersed by a magnetic prism to form spectra at energy losses of approximately 500-4000 cm^{-1} (60-500 meV), collected at every probe position as a 'spectrum image.' Figure 1(c) presents a map of two distinct vibrational EELS signatures (Figure 2(a)), separated by non-negative matrix factorization (NMF).[22,23] NMF is a blind source separation technique, a machine learning approach that unmixes signals contributing to a spectrum image.[20,24] NMF is one of several multivariate statistical approaches,[25] including principal component analysis (PCA) and independent component analysis (ICA), which seek a linear decomposition of a data-set into an alternative, simplified representation subject to particular assumptions or constraints. NMF makes only the physical assumptions that data are non-negative and that the entire spectrum image may be separated into a few spectral factors and their corresponding maps, i.e. the relative contribution of each signature at each probe position. Equivalent, albeit noisier, image contrast

was observed in maps obtained without recourse to machine learning algorithms by simply integrating the spectral signal within energy windows (Figure S1).

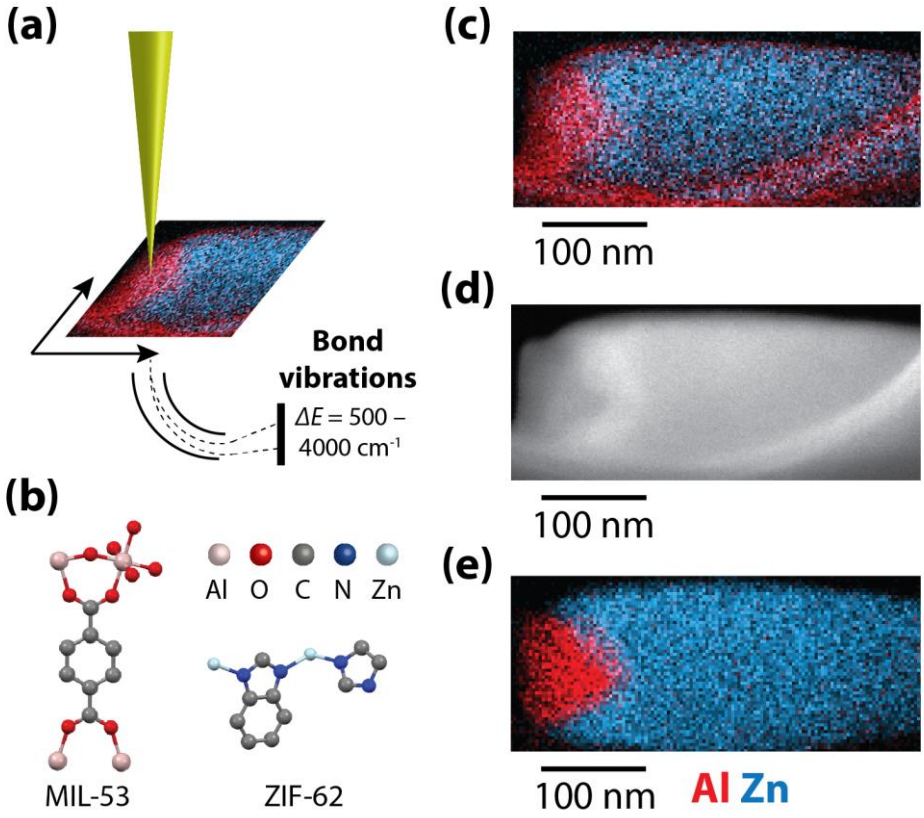

Figure 1. Correlated structural, elemental, and vibrational maps of a $(MIL\text{-}53)_{0.25}(a_gZIF\text{-}62)_{0.75}$ crystal-glass composite particle. (a) Schematic illustration of spatially resolved EELS at vibrational energies. (b), Structural fragments highlighting the key metal-organic bonding in MIL-53 and a_gZIF-62. Hydrogens are not shown for visual clarity. (c) Vibrational STEM-EELS signatures directly mapping the spatial variation in the carboxylate-terminated (MIL-53) and imidazolate (a_gZIF-62) organic linkers. (d) ADF-STEM micrograph and (e), STEM-EDS maps

at the Al and Zn K X-ray emission lines showing the location of metal centers (acquired after the STEM-EELS data).

Figure 1(d) presents correlated annular dark field (ADF) STEM obtained subsequently (that is, after completion of the vibrational EELS analysis) at 80 kV on a Thermo Fisher Osiris microscope (University of Cambridge, UK). The ADF-STEM micrograph shows characteristic mass-thickness contrast, where regions that have greater average mass or greater thickness appear brighter. The particle is supported on a lacey carbon film which appears at the bottom and lower right corner. The differences in atomic number between MIL-53, constructed from Al metal centers, and a_gZIF-62, constructed from heavier Zn metal centers, is suggested in the left-most side of the particle. Elemental mapping using STEM-EDS also corroborated the domain structure observed within the particles, depicted in Figure 1(e). The metal-center domain structure establishes that the red vibrational signature in Figure 1(c) is associated with the carboxylate ligands of the MIL-53 domain and that the blue signature is associated with the imidazolate-containing a_gZIF-62 glass. Replicate analyses of two additional particles are shown in Figures S2-S4 and STEM-EDS maps for C, N, and O are shown in Figures S5-S7.

Figure 2(a) shows the two spectral factors derived from NMF corresponding to the spatial maps in Figures 1(c). The number of factors used in NMF was determined by first performing a PCA decomposition on the data set, enabling the construction of a scree plot (Figure S8), used to assess the number of components or factors required to describe the majority of the variance in the data-set. In this case, five principal components were indicated. Then, NMF was performed separately, as its factors are not directly tied to their contribution to the variance, to explore the

number of factors necessary to give a complete representation without including factors describing noise in the data-set. In this case, five non-negative factors were also found to describe the data-set. A complete set of factors and maps is given in Figures S9-S12, including factors associated with the ZLP. Figure 3 plots the two factors of chemical interest. The factor associated with a_gZIF-62 showed peaks at 1500-1700 cm^{-1} (190-210 meV) and 2400 cm^{-1} (300 meV) with a small contribution at 3300 cm^{-1} (410 meV). The factor associated with MIL-53 showed a strong peak at 1300 cm^{-1} (160 meV) as well as at 3300 cm^{-1} (410 meV). The peaks at 3300 cm^{-1} (410 meV) provided spectroscopic evidence of hydrogen (C-H, N-H) recorded in the STEM-EELS data. Importantly, NMF can emphasize spectral differences where there is significant overlap in spectra rather than recovering complete physical spectra. This limitation does not preclude spatially resolved mapping using these fingerprints, but requires additional inspection of the as-recorded spectra.

Based on the NMF maps, the spatial resolution recorded in vibrational EELS of the CGC was estimated at <15 nm (80% criterion), assuming a sharp, edge-on interface (Figure 2(c)). The NMF maps provide spatial distributions for two vibrational fingerprints for ligand mapping, making use of the entire spectrum rather than a small energy range to reduce noise. Similar spatial resolution was apparent in energy filtered maps from the unprocessed spectrum image (Figure S1), where the domain boundary is distinct over 4-5 pixels (<15 nm). Dipole models for vibrational molecular signals suggest greater delocalization, but have not yet fully described the case of inelastic electron scattering in penetrating geometries.[3,9,26] Our results likely reflect the more localized excitation of molecular modes as opposed to lattice dynamics, although the contributions to localization arising from interface effects[5] or impact scattering[13] cannot be excluded.

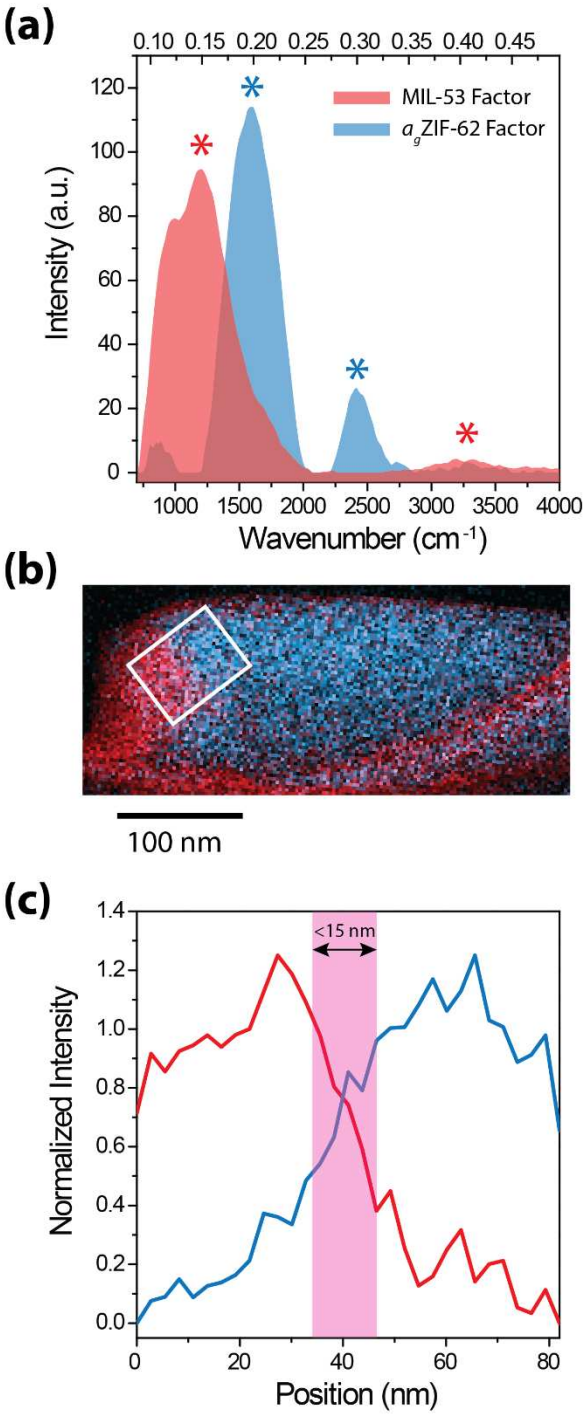

Figure 2. (a) NMF spectral factors associated with the MIL-53 and a_gZIF-62 phases in the MOF CGC with key spectral features marked. A complete set of factors and maps is shown in Figure S9. (b) The corresponding NMF map constructed from factors in (a) with an interface region

marked in white. (c) Intensity traces across the interface in the marked interface region used to estimate the spatial resolution from an integrated line profile, assuming an edge-on interface. The spatial resolution is estimated at <15 nm using the 80% criterion. The line profiles were normalized from 0 to 1 for comparison.

To understand the spectral information contained in the STEM-EELS data, Figure 3 presents spectra integrated within single-phase regions of the particle. Figure 2 and Figures S9-S12 depict the NMF spectral components showing similar features. However, NMF spectral factors represent components of the total spectrum at each pixel, and so the original spectra offer a clearer physical interpretation. The selected area spectra in Figure 3 were background subtracted, but otherwise represent minimally processed data. Spectra are shown for the particle shown in Figure 1 as well as a second particle. Selected area spectra for a third particle are shown in Figure S13 and spectra without background subtraction are presented in Figure S14. For the second particle in Figure 3(c)-(d), the recorded energy resolution was somewhat improved from approximately 25 meV (~200 cm^{-1}) to 20 meV (~160 cm^{-1}) by closing the energy selecting slit, at the expense of a poorer signal-to-noise ratio.

In Figure 3, the spectra from the a_gZIF-62 and the MIL-53 regions show significant intensity in the energy window from 1000-1700 cm^{-1} (120-210 meV), as expected for aromatic molecules containing heteroatom moieties. The spectrum from the a_gZIF-62 region, however, shows a maximum at 1500 cm^{-1} (190 meV) whereas the spectrum from the MIL-53 region has a maximum at 1300 cm^{-1} (160 meV). The spectrum from the ZIF-62 region further shows a unique peak at 2400 cm^{-1} (300 meV). These spectral differences are likewise shown for a third particle

in Figure S13. A small inflection at 3300 cm^{-1} (410 meV) is visible in the spectra from the first particle, although the noise reduction and separation from background features recovers this likely C-H and N-H vibrational band more clearly.

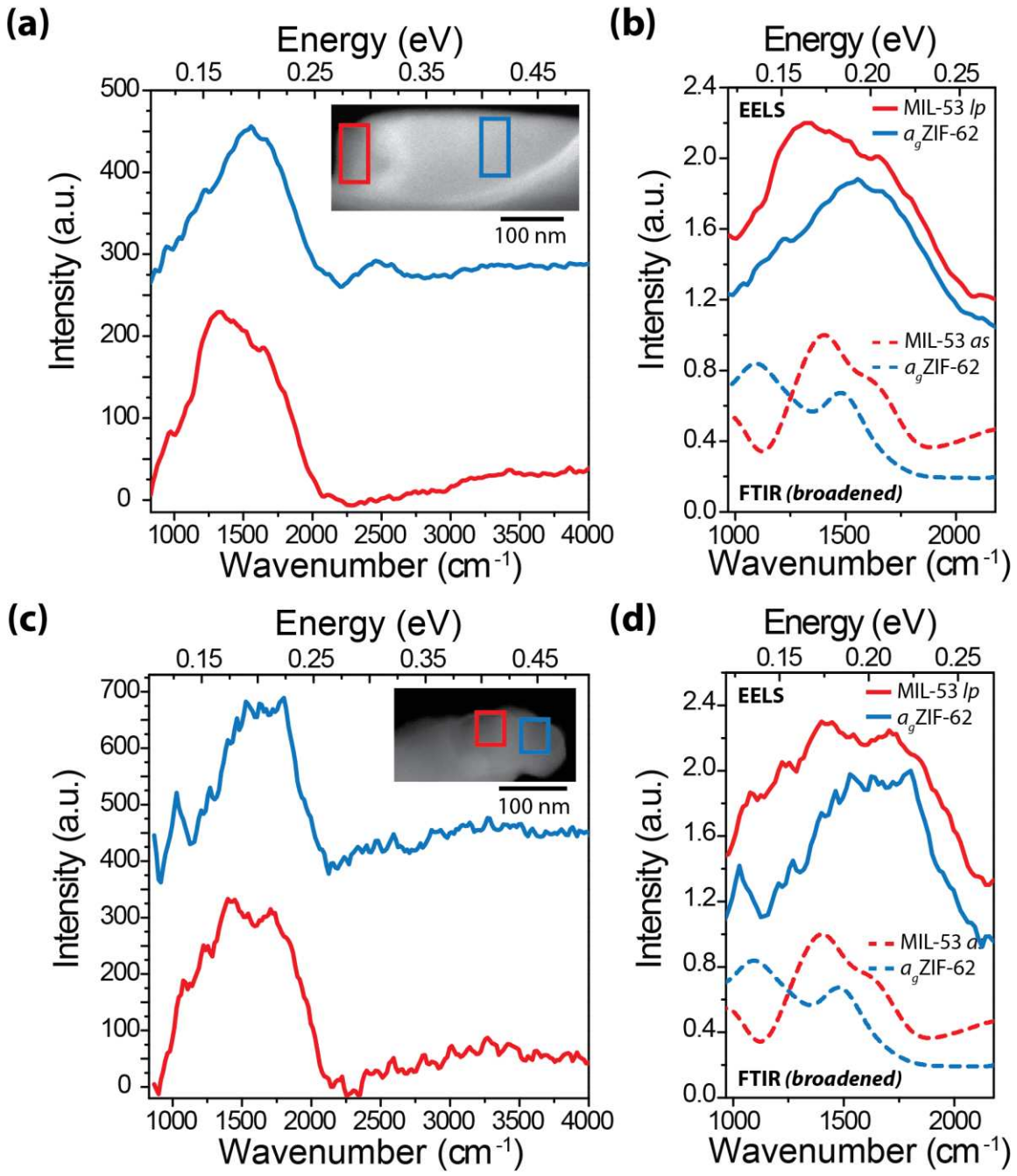

Figure 3. Comparison of local vibrational electron energy loss spectra. (a), (c) Experimental spectra integrated within selected areas marked on the inset for the particle shown in Figure 1 and a second particle (see also Figure S2). (b), (d) Comparisons with bulk FTIR spectra for MIL-53 *as* and a_gZIF-62, broadened to match the experimental EELS energy resolution. The spectra

in (a)-(b) were recorded with an energy resolution (including resolution loss due to instability during acquisition time) of approximately 25 meV (~200 cm^{-1}), and the spectra in (c)-(d) were obtained with an energy resolution of approximately 20 meV (~160 cm^{-1}) as described in the text. The designations MIL-53 *lp* and MIL-53 *as* refer to the large pore and the as synthesized phases of MIL-53, respectively.

To understand the origins of these signals, FTIR spectra from bulk a_gZIF-62 and the parent phase MIL-53 as synthesized (MIL-53 *as*) are shown in Figure 3 alongside the EEL spectra extracted from nanoscale volumes. In the composite, the high temperature MIL-53 large pore (MIL-53 *lp*) phase is stabilized,[19] which is suitably compared to the solvent stabilized MIL-53 *as* structure. The FTIR spectra were broadened by convolution with a Gaussian with a FWHM of 25 meV (~200 cm^{-1}) to match experimental conditions. The major features in the FTIR spectra are reproduced in the EEL spectra in the 1000-2000 cm^{-1} (120-250 meV) range. The feature at approximately 2400 cm^{-1} (300 meV) was attributed to overtones absent in FTIR based on inelastic neutron scattering (INS) of ZIFs closely related to ZIF-62.[27] The FTIR spectra, as acquired, are shown in Figure S15. The peak at approximately 1100 cm^{-1} (140 meV) observed in FTIR for a_gZIF-62 was not observed in EELS for the first particle, likely due to insufficient energy resolution to separate the feature from the tail of the zero loss peak. The feature was, however, recorded in the EEL spectra for the second particle, although due to its position on the ZLP tail distinguishing features from noise or fitting errors can be challenging. Spectra from electron beam trajectories outside the particle, also referred to as 'aloof' mode STEM-EELS, showed similar features, albeit with lower signal-to-noise ratio for an equivalent incident probe (Figure S16). Aloof spectra acquired first during spectrum image acquisition also provided a

reference spectrum for assessing any damage in the spectra recorded from within the particle. Relative intensities are not expected to be identical for EELS and IR spectroscopy due to differences in selection rules and excitation mechanisms, although similarities have been shown in previous experimental and calculated spectra.[3,26] Most notably, signals at low energies are lost or show modified signal amplitude due to difficulties in achieving a ZLP tail removal in the context of additional vibrational modes at far infrared and terahertz energies. The MIL-53 double peak also shows slightly different relative intensities between the two particles, and orientation-dependent effects, beam induced damage, or partial degradation of the sample during heat treatment to form the composite[19] cannot be ruled out. With advances in energy resolution and modelling, STEM-EELS may be able to examine whether some of these differences arise from local modulations in the bonding or composition of the MOF material, such as from missing linker defects. While small errors in the energy dispersion may introduce small offsets, and offsets of a few percent in energy between EELS and FTIR may be expected,[8] the spectra here show a striking resemblance with the major modes observed at the same energies.

The modes in this energy range can be further assigned using well-established practice in mid-IR spectroscopy based on literature as well as theory-based assignments. Based on INS experimental data and density functional theory (DFT) calculations of a series of ZIF crystals, the major modes in the 1000-2000 cm^{-1} (120-250 meV) window are C-C and C-N stretching modes of the aromatic rings with some contribution from C-H bending modes.[27] DFT calculations for IR and EEL spectra (Figures S17-S18) enabled assignment of the major modes contributing to peaks between 1000-2000 cm^{-1} (120-250 meV) as the symmetric and antisymmetric stretching modes of the carboxylate group, consistent with prior DFT calculations of IR spectra.[28] These assignments conclusively demonstrate that the differences in EELS

signatures observed reflect functional group specific differences between carboxylate and imidazolate linkers.

As a crucial control experiment to corroborate the vibrational EELS mapping of the ligand-associated functional groups, further EELS experiments were carried out at the C, N, and O *K* ionization edges (Figure 4). The electron beam was monochromated for analysis of the carbon *K* edge to enable fine structure analysis to complement the bonding information contained in the vibrational EELS data. Figure 4(a) shows significant differences in the C *K* edge fine structure, a signal that reflects predominantly the carbon projected density of states above the Fermi energy. The C *K* edge is conventionally interpreted as a signature of sp^3 and sp^2 content on the basis of the intensity at the π* and σ* energies at 284 eV and 291 eV, respectively.[29] Finer details reflect differences in energies of these broad categories of unoccupied electronic states and can be identified with particular functional groups, as for near edge fine structure in X-ray absorption spectroscopy. The C *K* spectrum from the MIL-53 domain shows three peaks in the energy window 284-290 eV, consistent with reported spectra for carboxylates.[30] The C *K* spectrum from the a_gZIF-62 domain shows a single bright peak at 285.5 eV, consistent with previous reports of core loss EELS of crystalline and amorphous ZIF-62[31] and with EELS of imidazole.[32] Previous work on ZIF-62 materials using STEM-EELS at higher electron beam doses likewise demonstrates that electron beam damage does not preclude EELS analysis of transitions at UV and visible energies.[20] These spectra provide further corroboration that the vibrational signals recorded from the domains arise from significant electronic structure differences in the two domains. However, this monochromated core loss analysis describes only the electronic states, and core ionization spectroscopy cannot access vibrational mode information due to the core-level state lifetimes. The vibrational STEM-EELS

results provide new insight into MOF composites by providing a direct signature of the intra-ligand bonds. Not only is this spectral signature comparable with benchtop spectroscopies like FTIR, it also presents opportunities for functional group mapping in systems with less distinctive core ionization fine structure. Here, the core loss analysis provides crucial evidence that the functional group signature of the ligands is not eliminated by electron beam induced damage. In addition to this validation experiment, no volume contraction associated with electron beam damage of MOFs[33] was recorded after vibrational and core loss STEM-EELS experiments (see also SI).

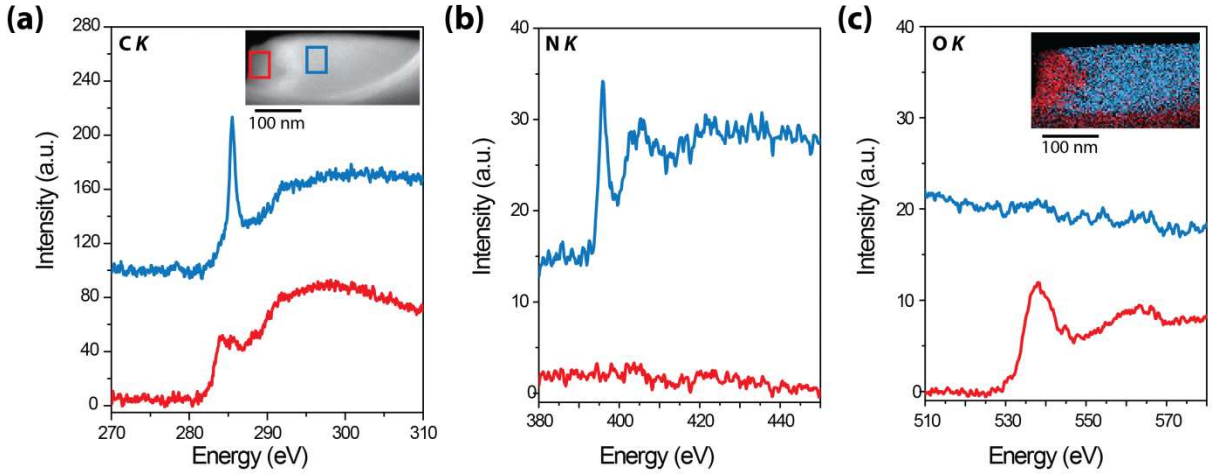

Figure 4. Spatially resolved fine structure at core loss ionization edges. (a) Background subtracted EELS at the C *K* edge integrated from selected areas (marked on the inset) for regions identified as MIL-53 (red) and a_gZIF-62 (blue). (b)-(c) EELS at the N *K* and O *K* ionization edges from corresponding regions, marked on the inset in (a). The inset in (c) shows maps derived from integration across the O *K* (red) and N *K* (blue) ionization edges.

EEL spectra at N and O *K* edges and the corresponding maps, shown in Figure 4(b), further illustrate the chemical domain structure inferred from the STEM-EDS analyses, but with enhanced detail highlighting, for example, the bright N π* peak consistent with imidazolate species.[31] The absence of any O *K* signal in the a_gZIF-62 domain and of any N *K* signal in the MIL-53 domain also provides strong evidence that the MOF domains are phase-pure away from the immediate vicinity of the interface, as the EELS signals in this energy range have significantly greater sensitivity than STEM-EDS data. Moreover, the inset map demonstrates the O and N signals provide a suitable signal to corroborate the chemical domain structure of the $(\text{MIL-53})_{0.25}(a_g\text{ZIF-62})_{0.75}$ particle. Notably, there is significant O *K* intensity in the lacey carbon, regions that are also highlighted in the vibrational map for the carboxylate-terminated linker molecules in MIL-53, strongly suggesting that, at the currently obtainable energy resolution in STEM-EELS, the vibrational maps are dominated by differences in C-N and C-O bonding interactions. Cumulatively, the identical domain structure observed across multiple spectroscopic measurements demonstrates conclusively that the vibrational EELS maps originate in the chemical differences between the two constituents of the composite.

Understanding domain structure in MOF composites, with known effects on the gas sorption[19,21] and mechanical properties,[31] requires techniques for monitoring the metal centers as well as the ligands. MOF glasses have been reported to exhibit a variety of liquid-phase mixing behaviours.[33,34] STEM-EELS mapping at vibrational energies establishes a route to independently track with nanometer spatial resolution the functional groups signatures of organic ligands in tandem with methods to assess mixing of metal centers. In the case of MOF CGCs, the sharpness of the interface constrains models for the mechanisms by which MOF CGCs stabilize

high temperature crystal phases,[19] improving the design of new composite materials with the processability of a glass.

These findings establish vibrational STEM-EELS as an essential spectroscopic technique for understanding organic and metal-organic microstructure with functional group sensitivity. Although many MOFs are prone to damage under electron beam irradiation, vibrational EELS offers another means to probe the molecular integrity of MOFs in electron microscopy. Further improvements in energy resolution will enhance the range of chemistries that can be spectroscopically and spatially resolved to understand the nanoscale organization of organic and metal-organic bonding and complex interfacial structures in emerging hybrid composite materials.

Methods. *Preparation of MOF CGCs.* Samples of $(\text{MIL-53})_{0.25}(a_g\text{ZIF-62})_{0.75}$ were prepared using precursor synthesis and processing methods as reported in Ref. 19.

Analytical scanning transmission electron microscopy. STEM-EELS and simultaneous ADF-STEM imaging data were acquired on a Hermes UltraSTEM 100MC microscope (Nion) equipped with a cold field emission gun electron source and an ultra-high resolution electron beam monochromator. The microscope was operated at 60 kV, while the electron optics were adjusted to a convergence angle of ~32 mrad and an electron probe <1 Å. For spectra at low energy losses, the monochromator slit was set to deliver a system electron energy spread of ~20-25 meV full-width at half-maximum at the zero loss peak (ZLP), resulting from the intrinsic energy spread at the exit plane of the monochromator as well as from instabilities during the exposure time to record spectra. Exposure times were selected to balance energy resolution and signal-to-noise ratio. For core loss spectra (*K* and *L* edges), the slit was opened to provide more

beam current due to the lower scattering cross sections at these higher energies. The microscope was equipped with a post-column Gatan Enfinium ERS dedicated spectrometer and coupling module to control collection for EELS, which was set to a collection of semi-angle of 44 mrad for both low and core loss measurements. EELS data were acquired in 'dualEELS' mode with near-simultaneous acquisition of the ZLP and a higher energy window, particularly necessary for exposure times sufficient to record vibrational EEL spectra with a suitable signal-to-noise ratio. Prior to microscopy at SuperSTEM, samples were baked in vacuum at approximately 140 °C for six hours. The dispersion (eV/channel) was adjusted in each spectral window according to the spectral range required. STEM-EDS and simultaneous ADF-STEM imaging data were acquired using an FEI Osiris microscope (Thermo Fisher Scientific) equipped with a high-brightness X-FEG electron source and operated at 80 kV. The beam convergence semi-angle was set to 11.0 mrad. EDS was acquired using a Super-X EDS detector system (Bruker) with four detectors mounted symmetrically about the optic axis of the microscope. STEM-EDS were acquired after STEM-EELS experiments.

Data Processing. Data were processed using Hyperspy,[35] an open-source software coded in Python. The spectra were first aligned using the ZLP. Initially, the spectral shifts were determined approximately by the maximum pixel intensity followed by a subpixel cross-correlation based routine. X-ray spikes on the CCD detector were removed by a routine that automatically identified outlying high-intensity pixels and then performed interpolation in the spectral region after the removal of the X-ray spike. NMF and ICA analyses were carried out as reported previously.[20,24] NMF was carried out using a project gradient method,[23] one of several possible implementation alternatives such as multiplicative update or least-squares approaches.[36] To determine the number of factors to retain in NMF, a PCA decomposition was performed first

to generate a scree plot (Figure S8). Then, NMF was separately carried out using the number of components determined from PCA as a starting point and with varying numbers of components to give a physically reasonable factorization with as few factors as possible associated with noise. Factors determined by NMF are not orthogonal like principal components and so give an alternative, but more physical representation as PCA often gives components with negative signal contributions. For selected area vibrational EEL spectra, background subtraction (removal of the ZLP tail contribution to the spectra) was performed using a Lorentzian function, using a multi-energy window approach using energy windows without chemical signals for fitting. These were determined by examination of NMF and ICA results as well as iterative refinement of the windows to minimize any spurious negative signals. Both the energy resolution (width of the ZLP) and the low energy cutoff in the dualEELS acquisition mode determined the energy window available for analysis. While not perfect, the Lorentzian model provides a sufficiently reasonable approximation of the ZLP tail in the vicinity of the fitting windows. An additional energy calibration correction was applied by acquiring dualEELS data with the ZLP recorded simultaneously to account for a systematic offset between the 'low' and 'high' energy windows. For selected area core loss EEL spectra, power law background fitting was used. For the precise determination of the recorded spatial resolution, a gold cross-grating replica image was used to calibrate the particle dimensions in the STEM images acquired with the EDS data.

Fourier-transform infrared absorption spectroscopy. Samples were finely ground and analyzed using a Bruker Tensor 27, scanning wavenumbers of 550–4000 cm^{-1} over 10 scans.

Density functional theory calculations. Density functional theory (DFT) calculations have been carried out using the Quantum Espresso package.[37] Additional details are given in the Supporting information. In brief, infrared absorption and electron energy loss spectra have been calculated

according to the formalisms described in Refs. [38] and [26], respectively. The IR spectrum was obtained using a Lorentzian broadening of 4 cm^{-1} FWHM. The EELS spectrum was calculated for an aloof beam geometry with an impact parameter of 5 nm and primary electron energy of 60 keV. The experimental energy resolution was accounted for using a broadening of 20 meV FWHM.

ASSOCIATED CONTENT

Supporting Information. The following files are available free of charge.

Additional figures illustrating further examples and alternative and supporting analyses for vibrational EELS, core ionization edge EELS, EDS, and FTIR reported in the main text and additional details on DFT calculations.

AUTHOR INFORMATION

Corresponding Author

*Email: smc204@cam.ac.uk

Present Addresses

[#]School of Chemical and Process Engineering and School of Chemistry, University of Leeds, Leeds LS2 9JT, United Kingdom

[⊥]School of Chemical Engineering, University of Queensland, St Lucia, QLD, 4072, Australia

Author Contributions

S.M.C., D.M.K., and Q.M.R carried out the electron microscopy experiments. S.M.C. performed the data processing. C.W.A. carried out the FTIR experiments. J.H. and C.W.A. synthesized the

materials. G.R. performed the DFT calculations. All authors contributed to the writing and revision of the manuscript. All authors have given approval to the final version of the manuscript.

Notes

The authors declare no competing financial interests.

ACKNOWLEDGMENT

S.M.C. acknowledges support from the Henslow Research Fellowship at Girton College, Cambridge and from a Goldstein Scholar Award from the Microanalysis Society. T.D.B. would like to thank the Royal Society for a University Research Fellowship (UF150021) and for a Research Grant (RG94426). J.H. and T.D.B. gratefully acknowledge the Engineering and Physical Sciences Research Council (EPSRC) for financial support under grant number EP/R015481/1. C.W.A. would like to thank the Royal Society for a PhD studentship (RG160498), and the Commonwealth Scientific and Industrial Research Council for additional support (C2017/3108). This work was granted access to the HPC resources of IDRIS under the allocation 2019-A0060910820 made by GENCI (Grand Equipement National de Calcul Intensif). P.A.M. thanks the EPSRC for financial support under grant number EP/R025517/1. SuperSTEM is the U.K. National Research Facility for Advanced Electron Microscopy, supported by the EPSRC.

REFERENCES

(1) Huth, F.; Chuvilin, A.; Schnell, M.; Amenabar, I.; Krutokhvostov, R.; Lopatin, S.; Hillenbrand, R. *Nano Lett.* **2013**, *13* (3), 1065–1072.
(2) Krivanek, O. L.; Lovejoy, T. C.; Dellby, N.; Aoki, T.; Carpenter, R. W.; Rez, P.; Soignard, E.; Zhu, J.; Batson, P. E.; Lagos, M. J.; et al. *Nature* **2014**, *514* (7521), 209–212.
(3) Rez, P.; Aoki, T.; March, K.; Gur, D.; Krivanek, O. L.; Dellby, N.; Lovejoy, T. C.; Wolf, S. G.; Cohen, H. *Nat. Commun.* **2016**, *7*, 10945.
(4) Lagos, M. J.; Trügler, A.; Hohenester, U.; Batson, P. E. *Nature* **2017**, *543* (7646), 529–532.
(5) Venkatraman, K.; Rez, P.; March, K.; Crozier, P. A. *Microscopy* **2018**, *67* (suppl_1), i14–i23.
(6) Crozier, P. A.; Aoki, T.; Liu, Q. *Ultramicroscopy* **2016**, *169*, 30–36.
(7) Haiber, D. M.; Crozier, P. A. *ACS Nano* **2018**, *12* (6), 5463–5472.
(8) Hachtel, J. A.; Huang, J.; Popovs, I.; Jansone-Popova, S.; Keum, J. K.; Jakowski, J.; Lovejoy, T. C.; Dellby, N.; Krivanek, O. L.; Idrobo, J. C. *Science* **2019**, *363* (6426), 525–528.
(9) Dwyer, C. *Phys. Rev. B* **2014**, *89* (5), 054103.
(10) Hage, F. S.; Nicholls, R. J.; Yates, J. R.; McCulloch, D. G.; Lovejoy, T. C.; Dellby, N.; Krivanek, O. L.; Refson, K.; Ramasse, Q. M. *Sci. Adv.* **2018**, *4* (6), eaar7495.
(11) Senga, R.; Suenaga, K.; Barone, P.; Morishita, S.; Mauri, F.; Pichler, T. *Nature* **2019**, 1–4.
(12) Hage, F. S.; Kepaptsoglou, D. M.; Ramasse, Q. M.; Allen, L. J. *Phys. Rev. Lett.* **2019**, *122* (1), 016103.
(13) Venkatraman, K.; Levin, B. D. A.; March, K.; Rez, P.; Crozier, P. A. *ArXiv181208895 Cond-Mat* **2018**.
(14) Vollmer, C.; Leitner, J.; Kepaptsoglou, D. M.; Ramasse, Q. M.; Busemann, H.; Hoppe, P. *Meteorit. Planet. Sci.* **2019**. https://doi.org/10.1111/maps.13389.
(15) Egerton, R. F. *Ultramicroscopy* **2015**, *159*, 95–100.
(16) Liu, G.; Chernikova, V.; Liu, Y.; Zhang, K.; Belmabkhout, Y.; Shekhah, O.; Zhang, C.; Yi, S.; Eddaoudi, M.; Koros, W. J. *Nat. Mater.* **2018**, *17* (3), 283–289.
(17) Bennett, T. D.; Horike, S. *Nat. Rev. Mater.* **2018**, *3* (11), 431.
(18) Bennett, T. D.; Yue, Y.; Li, P.; Qiao, A.; Tao, H.; Greaves, N. G.; Richards, T.; Lampronti, G. I.; Redfern, S. A. T.; Blanc, F.; et al. *J. Am. Chem. Soc.* **2016**, *138* (10), 3484–3492.
(19) Hou, J.; Ashling, C. W.; Collins, S. M.; Krajnc, A.; Zhou, C.; Longley, L.; Johnstone, D. N.; Chater, P. A.; Li, S.; Coulet, M.-V.; et al. *Nat. Commun.* **2019**, *10* (1), 1–10.
(20) Collins, S. M.; Kepaptsoglou, D. M.; Butler, K. T.; Longley, L.; Bennett, T. D.; Ramasse, Q. M.; Midgley, P. A. *J. Am. Chem. Soc.* **2018**, *140* (51), 17862–17866.
(21) Ashling, C. W.; Johnstone, D. N.; Widmer, R. N.; Hou, J.; Collins, S. M.; Sapnik, A. F.; Bumstead, A. M.; Midgley, P. A.; Chater, P. A.; Keen, D. A.; et al. *J. Am. Chem. Soc.* **2019**, *141* (39), 15641–15648.
(22) Lee, D. D.; Seung, H. S. *Nature* **1999**, *401* (6755), 788–791.
(23) Lin, C.-J. *Neural Comput.* **2007**, *19* (10), 2756–2779.
(24) Nicoletti, O.; de la Peña, F.; Leary, R. K.; Holland, D. J.; Ducati, C.; Midgley, P. A. *Nature* **2013**, *502* (7469), 80–84.
(25) Malinowski, E. R. *Factor Analysis in Chemistry*, 3 edition.; Wiley: New York, 2002.

(26) Radtke, G.; Taverna, D.; Lazzeri, M.; Balan, E. *Phys. Rev. Lett.* **2017**, *119* (2), 027402.
(27) Ryder, M. R.; Civalleri, B.; Bennett, T. D.; Henke, S.; Rudić, S.; Cinque, G.; Fernandez-Alonso, F.; Tan, J.-C. *Phys. Rev. Lett.* **2014**, *113* (21), 215502.
(28) Hoffman, A. E. J.; Vanduyfhuys, L.; Nevjestić, I.; Wieme, J.; Rogge, S. M. J.; Depauw, H.; Van Der Voort, P.; Vrielinck, H.; Van Speybroeck, V. *J. Phys. Chem. C* **2018**, *122* (5), 2734–2746.
(29) Egerton, R. F.; Whelan, M. J. *J. Electron Spectrosc. Relat. Phenom.* **1974**, *3* (3), 232–236.
(30) Alexander, C. M. O.; Cody, G. D.; De Gregorio, B. T.; Nittler, L. R.; Stroud, R. M. *Chem. Erde - Geochem.* **2017**, *77* (2), 227–256.
(31) Longley, L.; Collins, S. M.; Zhou, C.; Smales, G. J.; Norman, S. E.; Brownbill, N. J.; Ashling, C. W.; Chater, P. A.; Tovey, R.; Schönlieb, C.-B.; et al. *Nat. Commun.* **2018**, *9* (1), 2135.
(32) Apen, E.; Hitchcock, A. P.; Gland, J. L. *J. Phys. Chem.* **1993**, *97* (26), 6859–6866.
(33) Collins, S. M.; MacArthur, K. E.; Longley, L.; Tovey, R.; Benning, M.; Schönlieb, C.-B.; Bennett, T. D.; Midgley, P. A. *APL Mater.* **2019**, *7* (9), 091111.
(34) Longley, L.; Collins, S. M.; Li, S.; Smales, G. J.; Erucar, I.; Qiao, A.; Hou, J.; Cara M. Doherty; Thornton, A. W.; Hill, A. J.; et al. *Chem. Sci.* **2019**, *10*, 3592–3601.
(35) Francisco de la Peña; Tomas Ostasevicius; Vidar Tonaas Fauske; Pierre Burdet; Eric Prestat; Petras Jokubauskas; Magnus Nord; Mike Sarahan; Katherine E. MacArthur; Duncan N. Johnstone; et al. *Hyperspy/Hyperspy: HyperSpy 1.3.1*; Zenodo, 2018. https://doi.org/10.5281/zenodo.1221347.
(36) Berry, M. W.; Browne, M.; Langville, A. N.; Pauca, V. P.; Plemmons, R. J.. *Comput. Stat. Data Anal.* **2007**, *52* (1), 155–173.
(37) Giannozzi, P.; Baroni, S.; Bonini, N.; Calandra, M.; Car, R.; Cavazzoni, C.; Ceresoli, D.; Chiarotti, G. L.; Cococcioni, M.; Dabo, I.; et al. *J. Phys. Condens. Matter* **2009**, *21* (39), 395502.
(38) Balan, E.; Saitta, A. M.; Mauri, F.; Calas, G. *Am. Mineral.* **2001**, *86* (11–12), 1321–1330.

TOC GRAPHIC